Applied Mathematics and Computation 293 (2017) 320–333

Contents lists available at ScienceDirect

Applied Mathematics and Computation

journal homepage: www.elsevier.com/locate/amc

A multigrid solution for the Cahn–Hilliard equation on nonuniform grids

Yongho Choi, Darae Jeong, Junseok Kim*

Department of Mathematics, Korea University, Seoul 136-713, Republic of Korea

ARTICLE INFO

MSC:
65M55
65M06

Keywords:
Cahn–Hilliard equation
Nonuniform grid
Finite difference method
Multigrid method

ABSTRACT

We present a nonlinear multigrid method to solve the Cahn–Hilliard (CH) equation on nonuniform grids. The CH equation was originally proposed as a mathematical model to describe phase separation phenomena after the quenching of binary alloys. The model has the characteristics of thin diffusive interfaces. To resolve the sharp interfacial transition, we need a very fine grid, which is computationally expensive. To reduce the cost, we can use a fine grid around the interfacial transition region and a relatively coarser grid in the bulk region. The CH equation is discretized by a conservative finite difference scheme in space and an unconditionally gradient stable type scheme in time. We use a conservative restriction in the nonlinear multigrid method to conserve the total mass in the coarser grid levels. Various numerical results on one-, two-, and three-dimensional spaces are presented to demonstrate the accuracy and effectiveness of the nonuniform grids for the CH equation.

1. Introduction

We consider a nonlinear multigrid solution for the following Cahn–Hilliard (CH) equation on nonuniform grids:

$$\frac{\partial \phi(\mathbf{x},t)}{\partial t} = \Delta \mu(\phi(\mathbf{x},t)), \quad \mathbf{x} \in \Omega, \ t > 0, \tag{1}$$

$$\mu(\phi(\mathbf{x},t)) = F'(\phi(\mathbf{x},t)) - \epsilon^2 \Delta \phi(\mathbf{x},t), \tag{2}$$

where $\Omega \subset \mathrm{R}^d$ $(d = 1, 2, 3)$, ϕ is a conserved scalar field, $F(\phi) = 0.25(\phi^2 - 1)^2$, and ϵ is a positive constant. The CH equation was introduced to describe phase separation phenomena [1]. This equation arises from the Ginzburg–Landau free energy

$$\mathcal{E}(\phi) = \int_\Omega \left(F(\phi) + \frac{\epsilon^2}{2} |\nabla \phi|^2 \right) d\mathbf{x}. \tag{3}$$

The natural and no-flux boundary conditions are

$$\mathbf{n} \cdot \nabla \phi = \mathbf{n} \cdot \nabla \mu = 0 \text{ on } \partial\Omega, \text{ where } \mathbf{n} \text{ is a normal vector to } \partial\Omega. \tag{4}$$

* Corresponding author. Fax: +82 2 929 8562.
E-mail addresses: junseok_kim@yahoo.com (Y. Choi), cfdkim@korea.ac.kr (J. Kim).
URL: http://math.korea.ac.kr/~cfdkim (J. Kim)

http://dx.doi.org/10.1016/j.amc.2016.08.026
0096-3003/

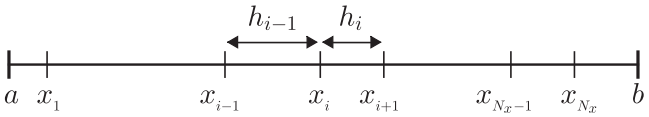

Fig. 1. Discretization of the domain with a nonuniform grid.

Then, we have

$$\frac{d}{dt}\mathcal{E}(\phi) = -\int_\Omega |\nabla\mu|^2 d\mathbf{x}, \tag{5}$$

$$\frac{d}{dt}\int_\Omega \phi d\mathbf{x} = 0, \tag{6}$$

where we used the no flux boundary condition Eq. (4). Therefore, the total energy is non-increasing and the total mass is conserved in time.

Most existing finite difference methods for the CH equation employed the uniform grid [2–8] or adaptive mesh refinement [9–11]. There are some cases which need non-square domains or adaptive mesh grids. Generally, adaptive mesh refinement technique is very complex to implement and even it is extremely difficulty to incorporate fluid flows into the CH equation. Various studies were performed on nonuniform grids to solve the Poisson [12,13], Euler [14,15], and Navier–Stokes [16,17] equations. However, to the authors' knowledge, the CH equation has not been solved using a multigrid method on nonuniform grids. Therefore, the main purpose of the present paper is to present a multigrid solution for solving the CH equation on nonuniform grids.

The remainder of this paper is organized as follows. In Section 2, we describe the numerical solution algorithm. The numerical results demonstrating the performance of the proposed algorithm on nonuniform grids are presented in Section 3. Finally, Section 4 gives our conclusions.

2. Numerical solution

2.1. Discretization

In this section, we discretize the CH equation on a nonuniform grid. For simplicity of exposition, we discretize the CH Eqs. (1) and (2) in one-dimensional space, i.e., $\Omega = (a, b)$. Two- and three-dimensional discretizations are defined analogously. Let x_i be the nonuniform grid points, that is, $x_i = x_{i-1} + h_{i-1}$ for $1 < i \le N_x$, where N_x is a positive even integer and h_i is the nonuniform grid-spacing as shown in Fig. 1.

Let ϕ_i^n and μ_i^n be approximations of $\phi(x_i, t_n)$ and $\mu(x_i, t_n)$, respectively. Here $t_n = (n-1)\Delta t$ and Δt is the time step. We discretize Eqs. (1) and (2) using the semi-implicit scheme and the nonlinear splitting algorithm [18]:

$$\frac{\phi_i^{n+1} - \phi_i^n}{\Delta t} = \Delta_d \mu_i^{n+1}, \quad 1 \le i \le N_x, \quad n \ge 0, \tag{7}$$

$$\mu_i^{n+1} = (\phi_i^{n+1})^3 - \phi_i^n - \epsilon^2 \Delta_d \phi_i^{n+1}, \tag{8}$$

where the discrete Laplacian is defined as $\Delta_d\phi_i = 2(\phi_{i+1} - \phi_i)/[h_i(h_i + h_{i-1})] - 2(\phi_i - \phi_{i-1})/[h_{i-1}(h_i + h_{i-1})]$. Here $h_0 = 2(x_1 - a)$ and $h_{N_x} = 2(b - x_{N_x})$. The Neumann boundary condition Eq. (4) is implemented as $\phi_0 = \phi_1$ and $\phi_{N_x+1} = \phi_{N_x}$. Let $\boldsymbol{\phi}^n = (\phi_1^n, \phi_2^n, \ldots, \phi_{N_x}^n)$ and $\mu^n = (\mu_1^n, \mu_2^n, \ldots, \mu_{N_x}^n)$. We define the discrete l_2-norm as

$$\|\boldsymbol{\phi}\|_2 = \sqrt{\sum_{1\le i\le N_x} \phi_i^2 \frac{h_{i-1} + h_i}{2}}. \tag{9}$$

We define the discrete energy functional by

$$\mathcal{E}_d(\boldsymbol{\phi}^n) = \sum_{i=1}^{N_x} F(\phi_i^n)\frac{h_{i-1} + h_i}{2} + \frac{\epsilon^2}{2}\sum_{i=1}^{N_x-1}\frac{(\phi_{i+1}^n - \phi_i^n)^2}{h_i}. \tag{10}$$

We also define the discrete total mass as

$$\mathcal{M}_d(\boldsymbol{\phi}^n) = \sum_{i=1}^{N_x} \phi_i^n \frac{h_{i-1} + h_i}{2}. \tag{11}$$

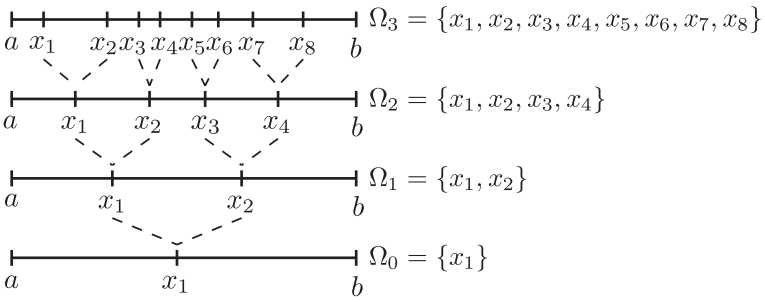

Fig. 2. Successively coarser grids when $N_x = 8$, Ω_k for $k = 3, 2, 1,$ and 0.

2.2. Multigrid method on a nonuniform grid

Next, we describe a nonlinear full approximation storage (FAS) multigrid method [19,20] to solve the nonlinear discrete system of (7) and (8). Let us rewrite Eqs. (7) and (8) as

$$N(\boldsymbol{\phi}^{n+1}, \mu^{n+1}) = (\mathbf{f}^n, \mathbf{g}^n), \tag{12}$$

where the nonlinear system operator N is defined as

$$N_i(\boldsymbol{\phi}^{n+1}, \mu^{n+1}) = \left(\frac{\phi_i^{n+1}}{\Delta t} - \Delta_d \mu_i^{n+1}, \mu_i^{n+1} - (\phi_i^{n+1})^3 + \epsilon^2 \Delta_d \phi_i^{n+1} \right)$$

and the source term is

$$(f_i^n,\ g_i^n) = \left(\frac{\phi_i^n}{\Delta t},\ -\phi_i^n \right).$$

Given $\{\boldsymbol{\phi}^n, \mu^n\}$, we want to calculate $\{\boldsymbol{\phi}^{n+1}, \mu^{n+1}\}$. We iterate the following FAS multigrid cycle until the discrete l_2-norm of the two consecutive approximations is less than a given tolerance, i.e., $\|\boldsymbol{\phi}^{n+1,m+1} - \boldsymbol{\phi}^{n+1,m}\|_2 < tol$. Let $\Omega_K = \{x_i | i = 1, \ldots, N_x\}$ be the original finest grid, where K satisfies $N_x = p \cdot 2^K$ and p is an odd number. Then, for $k = K, K-1, \ldots, 1$, we define successively coarser grids as $\Omega_{k-1} = \{y_i | y_i = 0.5(x_{2i-1} + x_{2i})$ and $x_{2i-1}, x_{2i} \in \Omega_k$ for $i = 1, \ldots, p \cdot 2^{k-1}\}$. Fig. 2 shows a schematic illustration of the discrete domains for $N_x = 8$ case.

We now introduce the multigrid iteration for solving the discretized problem Eq. (12) on grid level Ω_k.

$$\{\boldsymbol{\phi}_k^{n+1,m+1}, \mu_k^{n+1,m+1}\} = FAScycle(\boldsymbol{\phi}_k^{n+1,m}, \mu_k^{n+1,m}, N_k, \mathbf{f}_k^n, \mathbf{g}_k^n, \nu),$$

where $\{\boldsymbol{\phi}_k^{n+1,m}, \mu_k^{n+1,m}\}$ and $\{\boldsymbol{\phi}_k^{n+1,m+1}, \mu_k^{n+1,m+1}\}$ are the approximations of $\{\boldsymbol{\phi}^{n+1}, \mu^{n+1}\}$ before and after an FAS cycle. By starting from an initial value $\{\boldsymbol{\phi}^{n+1,0}, \mu^{n+1,0}\} = \{\boldsymbol{\phi}^n, \mu^n\}$, one step of the iteration is given in the following step:

Step 1) Presmoothing

$$\{\bar{\boldsymbol{\phi}}_k^{n+1,m},\ \bar{\mu}_k^{n+1,m}\} = SMOOTH^{\nu}(\boldsymbol{\phi}_k^{n+1,m}, \mu_k^{n+1,m}, N_k, \mathbf{f}_k^n, \mathbf{g}_k^n) \quad \text{on} \quad \Omega_k \text{ grid.}$$

This means performing ν smoothing steps with the initial approximations $\boldsymbol{\phi}_k^{n+1,m}$, $\mu_k^{n+1,m}$, source terms $\mathbf{f}_k^n, \mathbf{g}_k^n$, and *SMOOTH* relaxation operator to get the approximations $\bar{\boldsymbol{\phi}}_k^{n+1,m}, \bar{\mu}_k^{n+1,m}$. First, let us discretize Eq. (7) as a Gauss–Seidel type.

$$\frac{\phi_i^{n+1,m,s+1}}{\Delta t} + \frac{2}{h_i h_{i-1}} \mu_i^{n+1,m,s+1} = f_i^n + \frac{2}{h_i(h_i + h_{i-1})} \mu_{i+1}^{n+1,m,s} + \frac{2}{h_{i-1}(h_i + h_{i-1})} \mu_{i-1}^{n+1,m,s+1}, \tag{13}$$

Here, the indices s and $s+1$ denote the current and the new approximations. Next, let us discretize Eq. (8). Since $(\phi_i^{n+1,m,s+1})^3$ is nonlinear term, we linearize it at $\phi_i^{n+1,m,s}$, i.e.,

$$(\phi_i^{n+1,m,s+1})^3 \approx (\phi_i^{n+1,m,s})^3 + 3(\phi_i^{n+1,m,s})^2(\phi_i^{n+1,m,s+1} - \phi_i^{n+1,m,s}).$$

Therefore, Eq. (8) can be rewritten as

$$-\left(\frac{2\epsilon^2}{h_i h_{i-1}} + 3(\phi_i^{n+1,m,s})^2 \right) \phi_i^{n+1,m,s+1} + \mu_i^{n+1,m,s+1} = g_i^n - 2(\phi_i^{n+1,m,s})^3$$
$$- \frac{2\epsilon^2}{h_i(h_i + h_{i-1})} \phi_{i+1}^{n+1,m,s} - \frac{2\epsilon^2}{h_{i-1}(h_i + h_{i-1})} \phi_{i-1}^{n+1,m,s+1}. \tag{14}$$

One *SMOOTH* relaxation operator step consists of solving the system Eqs. (13) and (14) by 2×2 matrix inversion for each i on Ω_k grid. After taking ν smoothing steps, we let $\{\bar{\boldsymbol{\phi}}_k^{n+1,m},\ \bar{\mu}_k^{n+1,m}\}$

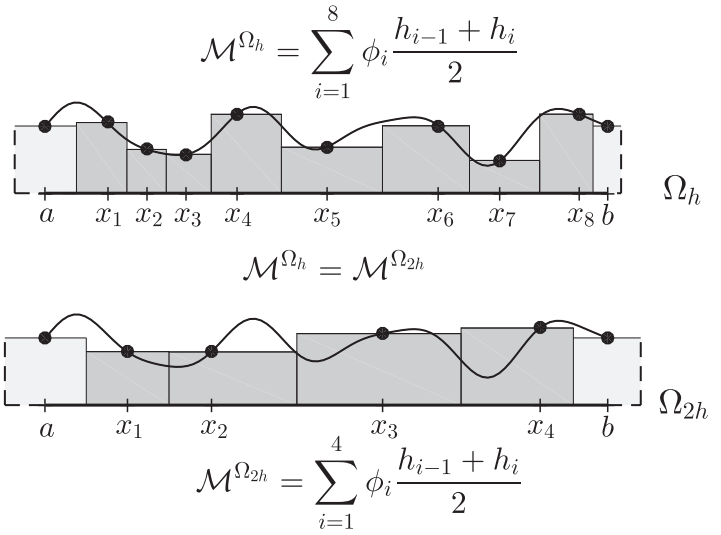

Fig. 3. Illustration for conservative restriction from Ω_h to Ω_{2h}.

Step 2) Compute the defect

$$(\alpha_k, \beta_k) = (\mathbf{f}_k^n, \mathbf{g}_k^n) - N_k(\bar{\boldsymbol{\phi}}_k^{n+1,m}, \bar{\mu}_k^{n+1,m}). \tag{15}$$

Step 3) Restrict the defect and $\{\bar{\boldsymbol{\phi}}_k^{n+1,m},\ \bar{\mu}_k^{n+1,m}\}$

$$(\alpha_{k-1}, \beta_{k-1}) = I_k^{k-1}(\alpha_k, \beta_k), \quad (\bar{\boldsymbol{\phi}}_{k-1}^{n+1,m}, \quad \bar{\mu}_{k-1}^{n+1,m}) = I_k^{k-1}(\bar{\boldsymbol{\phi}}_k^{n+1,m}, \quad \bar{\mu}_k^{n+1,m}).$$

The conservative restriction: to preserve the mass conservation property, we apply the following conservative restriction (see Fig. 3):

$$\begin{aligned}\alpha_{k-1}(i) &= I_k^{k-1}\alpha_k(i)\\ &= \left(\alpha_k(2i-1)\frac{h_{2i-2}^k + h_{2i-1}^k}{2} + \alpha_k(2i)\frac{h_{2i-1}^k + h_{2i}^k}{2}\right) \Big/ \left(\frac{h_{i-1}^{k-1} + h_i^{k-1}}{2}\right),\end{aligned}$$

where $\boldsymbol{\alpha}_k(i)$ is the ith component of the vector $\boldsymbol{\alpha}_k$. β_{k-1} also can be similarly defined and the restriction operator I_k^{k-1} maps k-level functions to $(k-1)$-level functions.

Step 4) Compute the right-hand side

$$(\mathbf{f}_{k-1}^n, \mathbf{g}_{k-1}^n) = (\alpha_{k-1}, \beta_{k-1}) + N_{k-1}(\bar{\boldsymbol{\phi}}_{k-1}^{n+1,m}, \bar{\mu}_{k-1}^{n+1,m}).$$

Step 5) Compute an approximate solution $\{\hat{\phi}_{k-1}^{n+1,m}, \quad \hat{\mu}_{k-1}^{n+1,m}\}$ of the coarse grid equation on Ω_{k-1}, i.e.,

$$N_{k-1}(\boldsymbol{\phi}_{k-1}^{n+1,m}, \mu_{k-1}^{n+1,m}) = (\mathbf{f}_{k-1}^n, \mathbf{g}_{k-1}^n). \tag{16}$$

If $k = 1$, we apply the *SMOOTH* relaxation operator. If $k > 1$, we solve Eq. (16) by performing an FAS k-grid cycle using $\{\bar{\phi}_{k-1}^{n+1,m},\ \bar{\mu}_{k-1}^{n+1,m}\}$ as an initial approximation:

$$\{\hat{\phi}_{k-1}^{n+1,m}, \hat{\mu}_{k-1}^{n+1,m}\} = \text{FAS cycle}(\bar{\phi}_{k-1}^{n+1,m}, \bar{\mu}_{k-1}^{n+1,m}, N_{k-1}, \mathbf{f}_{k-1}^n, \mathbf{g}_{k-1}^n, \nu).$$

Step 6) Compute the coarse grid correction (CGC)

$$\hat{\mathbf{v}}_{k-1}^{n+1,m} = \hat{\phi}_{k-1}^{n+1,m} - \bar{\phi}_{k-1}^{n+1,m}, \quad \hat{\mathbf{w}}_{k-1}^{n+1,m} = \hat{\mu}_{k-1}^{n+1,m} - \bar{\mu}_{k-1}^{n+1,m}.$$

Step 7) Interpolate the correction

$$\hat{\mathbf{v}}_k^{n+1,m} = I_{k-1}^k \hat{\mathbf{v}}_{k-1}^{n+1,m}, \quad \hat{\mathbf{w}}_k^{n+1,m} = I_{k-1}^k \hat{\mathbf{w}}_{k-1}^{n+1,m}.$$

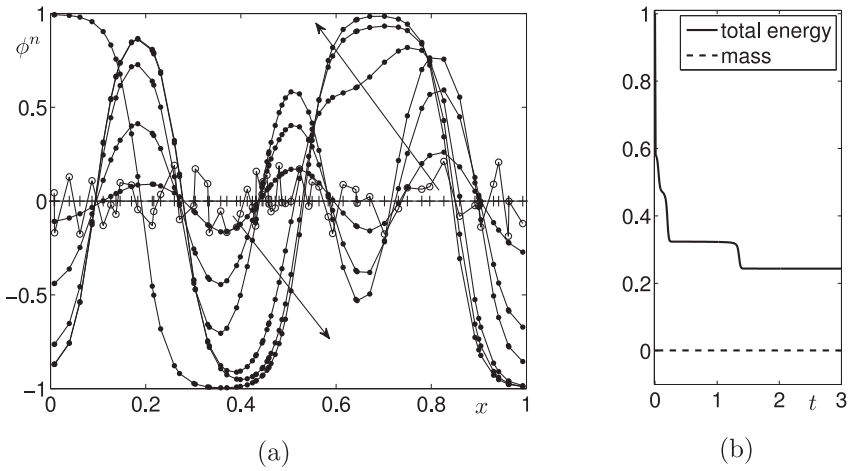

Fig. 4. (a) Evolution of the initial concentration $\phi(x,0) = 0.1\text{rand}(\ )$. Here, the arrows represent the direction of the increasing time. (b) Evolution of the discrete normalized total energy $\mathcal{E}_d(\boldsymbol{\phi}^n)/\mathcal{E}_d(\boldsymbol{\phi}^0)$ (solid line) and the total mass (dashed line).

Here, the coarse values are simply transferred to the two closet fine grid points, i.e., $\mathbf{v}_k(2i) = \mathbf{v}_k(2i-1) = I_{k-1}^k \mathbf{v}_{k-1}(i) = \mathbf{v}_{k-1}(i)$ for $1 \le i \le p \cdot 2^{k-1}$.

Step 8) Compute the corrected approximation on Ω_k

$$\boldsymbol{\phi}_k^{n+1,m,\ \text{after CGC}} = \bar{\boldsymbol{\phi}}_k^{n+1,m} + \hat{\mathbf{v}}_k^{n+1,m},$$
$$\mu_k^{n+1,m,\ \text{after CGC}} = \bar{\mu}_k^{n+1,m} + \hat{\mathbf{w}}_k^{n+1,m}.$$

Step 9) Postsmoothing

$$\{\phi_k^{n+1,m+1}, \mu_k^{n+1,m+1}\} = SMOOTH^{\nu}(\phi_k^{n+1,m,\ \text{after CGC}}, \mu_k^{n+1,m,\ \text{after CGC}}, N_k, \mathbf{f}_k^n, \mathbf{g}_k^n).$$

This completes the description of a nonlinear FAS cycle. More details can be found in [19,20].

3. Numerical results

We perform all the numerical tests on Intel(R) Core(TM) i5-2320 CPU @ 3.00 GHz.

3.1. One-dimensional space

3.1.1. Spinodal decomposition

First, we perform a spinodal decomposition using the CH equation on a randomly distributed nonuniform grid in the one-dimensional domain $\Omega = (0,1)$. The initial condition is set to be $\phi(x,0) = 0.2\text{rand}()$, where rand() is uniformly distributed random number between -1 and 1. With this initial condition, we examine the evolution of ϕ^n on the nonuniform mesh. In this test, we take $\epsilon = 0.0375$, $N_x = 64$, $\Delta t = 0.01$, and $T = 3$. The numerical solutions are shown in Fig. 4(a), where arrows indicate the direction of increasing time. The normalized total energy $\mathcal{E}_d(\boldsymbol{\phi}^n)/\mathcal{E}_d(\boldsymbol{\phi}^0)$ and the total mass with respect to time t are plotted in Fig. 4(b). These results confirm that the total energy is non-increasing and the total mass is conserved.

3.1.2. Resolving the sharp interfacial transition

To demonstrate the efficiency of the nonuniform multigrid method, we present an example with the following initial condition on $\Omega = (0,1)$:

$$\phi(x,0) = \begin{cases} 1, & \text{if} \quad 0.31 < x < 0.69 \\ -1, & \text{otherwise.} \end{cases}$$

In this test, we use three different grids such as uniform grids with $N_x = 16$, $N_x = 144$, and a nonuniform grid with $N_x = 32$. A time step size $\Delta t = 0.01$ and $\epsilon = 0.0075$ in Fig. 5 are used. Fig. 5(a)–(c) represent the numerical solution ϕ^n at $T = 1$ on the uniform grids with $N_x = 16$, $N_x = 144$, and a nonuniform grid with $N_x = 32$, respectively. When we use the finer uniform grid, we can obtain the well-resolved interfacial transition than the coarser grid. Using a nonuniform grid with $N_x = 32$, we get a comparable result to the finest uniform grid with $N_x = 144$ (see Fig. 5(d)). These results demonstrate the effectiveness and efficiency of the nonuniform grid for sharp interfacial transition problems.

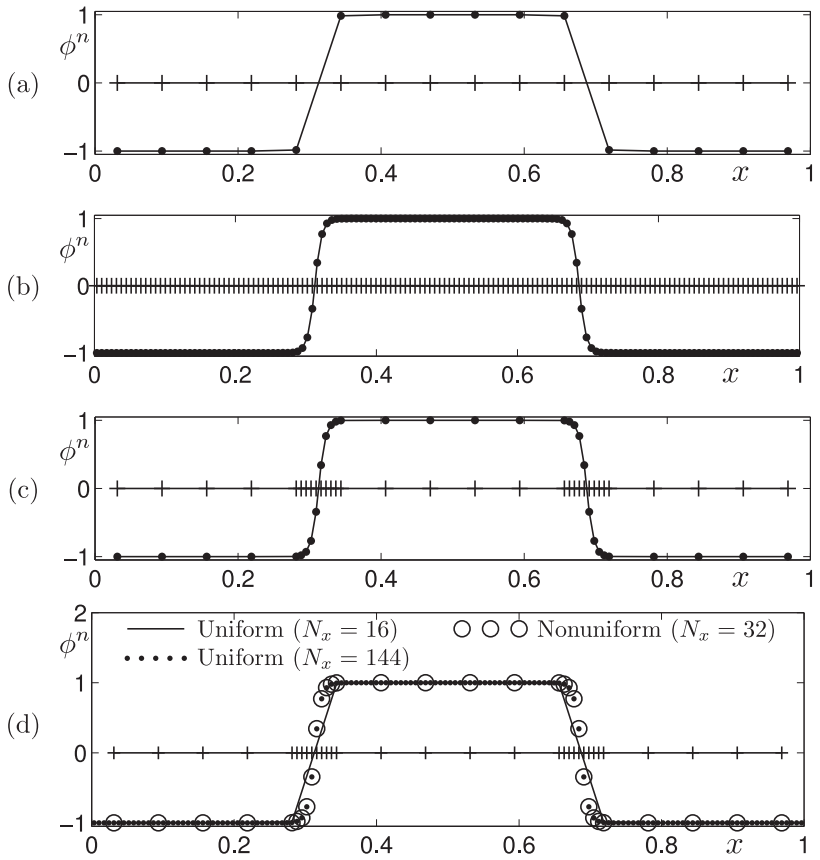

Fig. 5. Numerical results on three different grids: (a) uniform grid with $N_x = 16$, (b) $N_x = 144$, and (c) nonuniform grid with $N_x = 32$ on $\Omega = (0, 1)$. (d) Three overlapped numerical results at $T = 1$. $\Delta t = 0.01$ and $\epsilon = 0.0075$ are used.

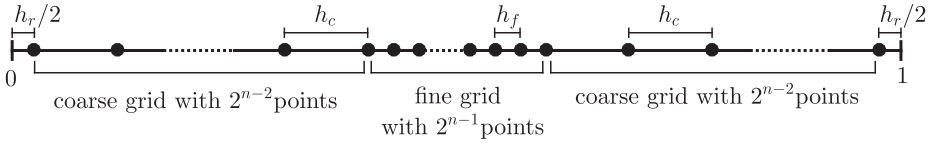

Fig. 6. Schematic illustration of a nonuniform grid on $\Omega = (0, 1)$ for convergence test.

3.2. Convergence test

In this section, we investigate the convergence and accuracy of numerical solution with nonuniform multigrid method.

For the convergence test, the nonuniform spatial grid is composed of 2^n points. Here, the coarse grid over the whole discrete domain has equidistant grid-spacing $h_c = (0.8 - h_r)/2^{n-1}$ and the fine grid has equidistant grid-spacing $h_f = 0.2/(2^{n-1} - 1)$ on [0.4, 0.5]. Specifically, we put the fine grid across the diffuse interface. This nonuniform grid is illustrated in Fig. 6.

In this test, we fix the parameter $\epsilon = 0.0300187$ and set the following initial condition as

$$\phi(x, 0) = 0.9 \tanh((x - 0.5)/(2\sqrt{2}\epsilon))$$

on the computational domain $\Omega = (0, 1)$.

Since there is no closed-form analytic solution for this problem, we consider a reference numerical solution, ϕ^{ref}, which is obtained with very fine spatial step h_r and temporal step Δt_r. Then, we denote the error by $e := \phi - \phi^{\text{ref}}$. The convergence rate is defined as the ratio of successive errors, $\log_2(\|e_{N_x}\|_2/\|e_{N_x/2}\|_2)$. Here, $\|e_{N_x}\|_2$ is measured by the discrete l_2-norm.

To verify the convergence of numerical solution with respect to spatial grid, we obtain the numerical solutions on the defined nonuniform grids with 2^n points when $n = 4, 5, 6$ and 7. In all cases, we use the time step size $\Delta t = 1.0\text{e}{-6}$ and the total time $T = 0.001$. The reference solution is evaluated with $h_r = 1/4096$ and $\Delta t_r = 1.0\text{e}{-6}$ on uniform spatial grid. We measure the error between the reference solution and the numerical solution on each grid by using the linear interpolation.

Table 1 lists the discrete l_2-norm of errors and convergence rates with respect to different spatial step sizes. The results suggest that the proposed numerical method is second-order accurate in space.

Table 1
Convergence test with respect to spatial step size.

N_x	16	Rate	32	Rate	64	Rate	128
$\|e_{N_x}\|_2$	4.8213e−3	1.959	1.2399e−3	2.017	3.0630e−4	2.021	7.5478e−5

Table 2
Convergence test with respect to time step size.

N_t	10	Rate	20	Rate	40	Rate	80
$\|e_{N_t}\|_2$	6.0342e−3	0.981	3.0563e−3	0.992	1.5367e−3	0.971	7.8405e−4

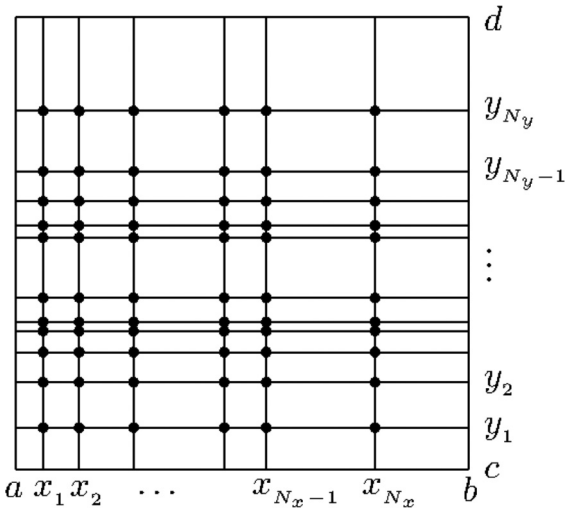

Fig. 7. Schematic illustration of a nonuniform grid on the two-dimensional space $\Omega = (a, b) \times (c, d)$.

Now, we investigate the accuracy of numerical solution with respect to time step size. For this, we consider the four different time step sizes $\Delta t = 0.01/2^n$ for $n = 0, 1, 2,$ and 3. And the numerical solution is solved up to time $T = 0.1$. In all tests, we use the nonuniform grid in the previous test with $N_x = 256$. The reference solution ϕ^{ref} is set by the numerical solution at $T = 0.1$ with $\Delta t_r = 1.0\text{e-}6$ and $N_x = 256$ on the nonuniform grid.

Table 2 represents the discrete l_2-norm of errors and convergence rates with respect to different time step sizes. For smaller Δt, we can see that the rate of convergence is first-order.

3.3. Two-dimensional space

We discretize Eqs. (1) and (2) in time by a nonlinear splitting algorithm on a nonuniform grid (see Fig. 7):

$$\frac{\phi_{ij}^{n+1} - \phi_{ij}^{n}}{\Delta t} = \Delta_d \mu_{ij}^{n+1}, \ \ 1 \le i \le N_x, \ \ 1 \le j \le N_y, \ \ n \ge 0, \tag{17}$$

$$\mu_{ij}^{n+1} = (\phi_{ij}^{n+1})^3 - \phi_{ij}^{n} - \epsilon^2 \Delta_d \phi_{ij}^{n+1}, \tag{18}$$

where the discrete Laplacian is defined as

$$\Delta_d \phi_{ij} = \frac{2(\phi_{i+1,j} - \phi_{ij})}{h_i^x (h_i^x + h_{i-1}^x)} - \frac{2(\phi_{ij} - \phi_{i-1,j})}{h_{i-1}^x (h_i^x + h_{i-1}^x)} + \frac{2(\phi_{i,j+1} - \phi_{ij})}{h_j^y (h_j^y + h_{j-1}^y)} - \frac{2(\phi_{ij} - \phi_{i,j-1})}{h_{j-1}^y (h_j^y + h_{j-1}^y)}.$$

Here, h_i^x and h_j^y are nonuniform space step sizes in the x- and y-directions, respectively.

We define the discrete energy functional $\mathcal{E}_d$ and the total mass $\mathcal{M}_d$ by

$$\mathcal{E}_d(\boldsymbol{\phi}^n) = \frac{1}{4} \sum_{i=1}^{N_x} \sum_{j=1}^{N_y} F(\phi_{ij}^n)(h_{i-1}^x + h_i^x)(h_{j-1}^y + h_j^y) + \frac{\epsilon^2}{2} \sum_{i=1}^{N_x - 1} \sum_{j=1}^{N_y - 1} \left[\frac{h_j^y}{h_i^x} (\phi_{i+1,j}^n - \phi_{ij}^n)^2 + \frac{h_i^x}{h_j^y} (\phi_{i,j+1}^n - \phi_{ij}^n)^2 \right], \tag{19}$$

$$\mathcal{M}_d(\phi^n) = \frac{1}{4} \sum_{i=1}^{N_x} \sum_{j=1}^{N_y} \phi_{ij}^n (h_{i-1}^x + h_i^x)(h_{j-1}^y + h_j^y). \tag{20}$$

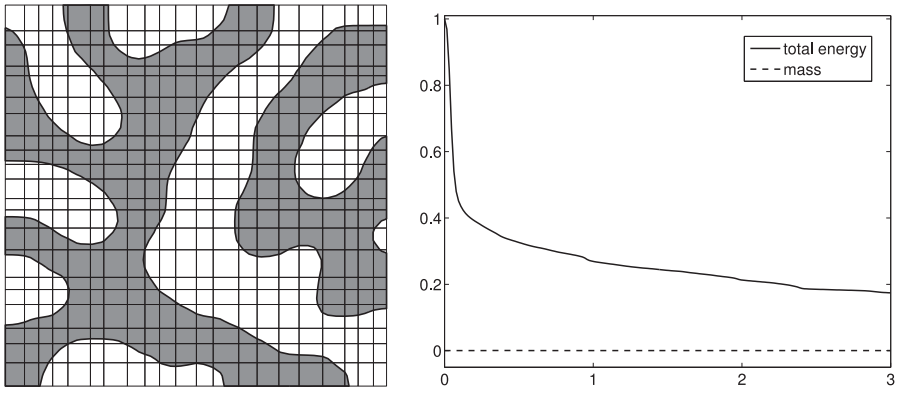

Fig. 8. Spinodal decomposition on a square domain. (a) A snapshot of ϕ at $t = 20\Delta t$ with the initial condition $\phi(x, y, 0) = 0.1\text{rand}(\ )$. (b) Temporal evolutions of the normalized discrete total energy $\mathcal{E}_d(\boldsymbol{\phi}^n)/\mathcal{E}_d(\boldsymbol{\phi}^0)$ (solid line) and the total mass (dashed line) of the numerical solutions.

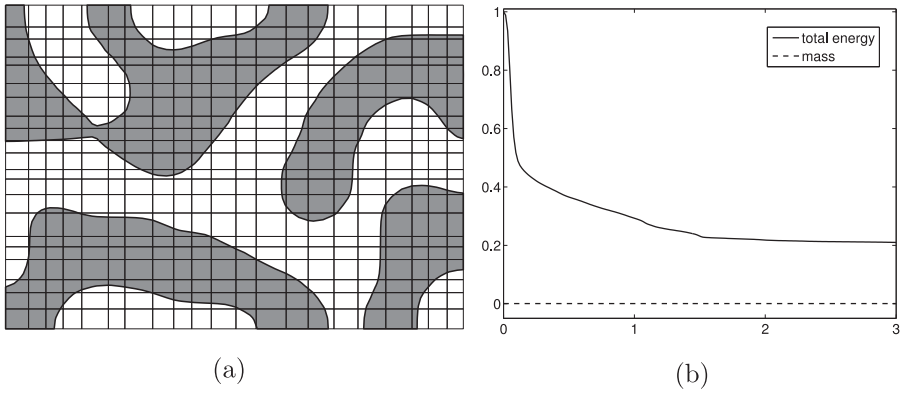

Fig. 9. Spinodal decomposition on a non-square domain. (a) A snapshot of ϕ at $t = 20\Delta t$ with the initial condition $\phi(x, y, 0) = 0.1\text{rand}(\ )$. (b) Temporal evolutions of the normalized discrete total energy $\mathcal{E}_d(\boldsymbol{\phi}^n)/\mathcal{E}_d(\boldsymbol{\phi}^0)$ (solid line) and the total mass (dashed line) of the numerical solutions.

3.3.1. Spinodal decomposition

To confirm that the proposed algorithm can operate on a two-dimensional nonuniform grid, we perform spinodal decomposition simulation on a square domain $\Omega = (0, 1) \times (0, 1)$. A mesh of 64×64 grid points, $\Delta t = 1/64$, and $\epsilon = 0.0156$ are used with a randomly distributed nonuniform grid spacing. Fig. 8(a) shows a snapshot of ϕ at $t = 20\Delta t$ with the initial condition $\phi(x, y, 0) = 0.1\text{rand}(\ )$, where rand() is a random number between -1 and 1. Fig. 8(b) shows temporal evolutions of the normalized discrete total energy $\mathcal{E}_d(\boldsymbol{\phi}^n)/\mathcal{E}_d(\boldsymbol{\phi}^0)$ (solid line) and the discrete total mass $\mathcal{M}_d(\boldsymbol{\phi}^n)$ (dashed line) of the numerical solutions. We can observe that the energy is decreasing and the total mass is conserved.

We also perform a spinodal decomposition simulation on a non-square domain $\Omega = (0, \sqrt{2}) \times (0, 1)$ (see Fig. 9). The other parameters are the same in the simulation for Fig. 8.

3.3.2. Locally refined 2D grid

We perform a numerical simulation on a locally refined grid as shown in Fig. 10(a) to highlight the usefulness of the nonuniform grid. Fig. 10(b) represents a magnified view of the marked part in Fig. 10(a). Here, the larger grid size is $h = 1/16$ and the smaller grid size is $h = 1/512$.

A numerical test is performed on $\Omega = (0, 1) \times (0, 1)$ with a 64×64 grid, $\Delta t = 0.0001$, and total simulation time $T = 0.01$. Across the interfacial regions, the concentration field varies from -0.9 to 0.9 over a distance of approximately $2\sqrt{2}\epsilon \tanh^{-1}(0.9)$. Therefore, if we want this value to be approximately m grid points, the ϵ value needs to be taken as follows [21]:

$$\epsilon = \epsilon_m = \frac{hm}{2\sqrt{2}\tanh^{-1}(0.9)}. \tag{21}$$

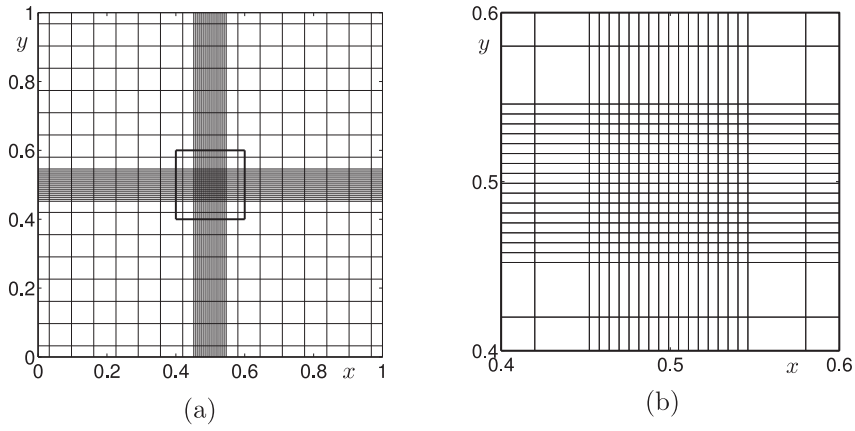

Fig. 10. (a) Locally refined 2D grid. Here, the larger grid size is $h = 1/16$ and the smaller grid size is $h = 1/512$. (b) Magnified view of the boxed region in (a).

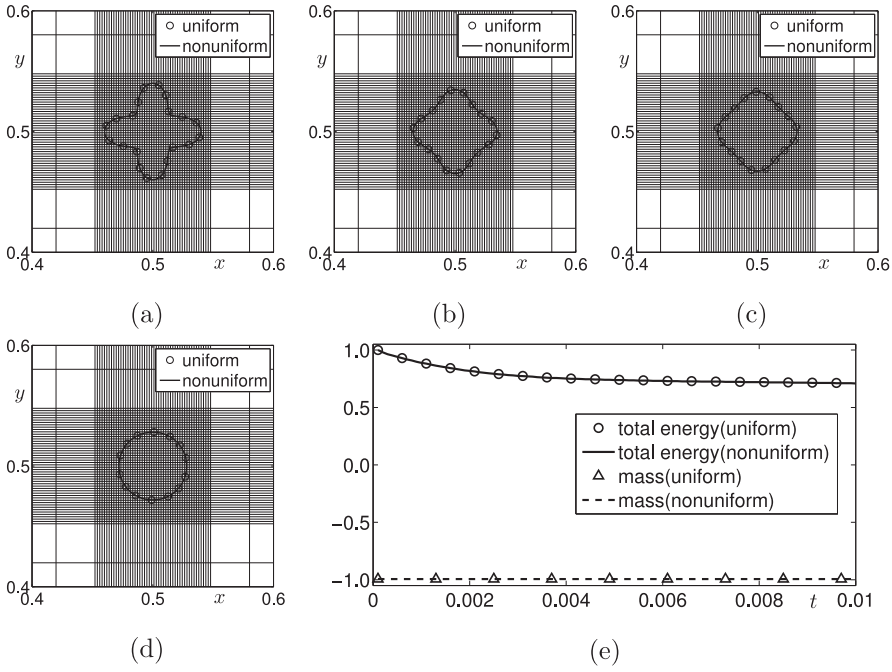

Fig. 11. (a)–(d) Snapshots of ϕ at (a) $t = 0$, (b) $t = 20\Delta t$, (c) $t = 30\Delta t$, and (d) $t = 100\Delta t$. (e) Temporal evolutions of the normalized discrete total energy $\mathcal{E}_d(\boldsymbol{\phi}^n)/\mathcal{E}_d(\boldsymbol{\phi}^0)$ and the total mass of the numerical solutions.

We use $\epsilon = 4h/[2\sqrt{2}\tanh^{-1}(0.9)]$, where h is the finer grid size, i.e., $h = 1/512$. For this test, we use the following the initial condition:

$$\phi(x, y, 0) = \tanh\frac{0.04 + 0.01\cos(4\theta) - \sqrt{(x-0.5)^2 + (y-0.5)^2}}{\sqrt{2}\epsilon},$$

where

$$\theta = \begin{cases} \tan^{-1}\left(\dfrac{y-0.5}{x-0.5}\right), & \text{if } x > 0.5 \\ \pi + \tan^{-1}\left(\dfrac{y-0.5}{x-0.5}\right), & \text{otherwise.} \end{cases}$$

Here, we use $\epsilon = 0.001876$ and $\Delta t = 0.0001$. Fig. 11 represents the evolution of a four-fold shaped interface on the uniform grid ($h = 1/512$) and the nonuniform grid which is defined in Fig. 10. In Fig. 11(a)–(d), the initial star shape deforms to a circular shape over time. The figures show that the results from the two grid systems are almost identical. Fig. 11(e) confirms that the total energy decreases and mass is conserved.

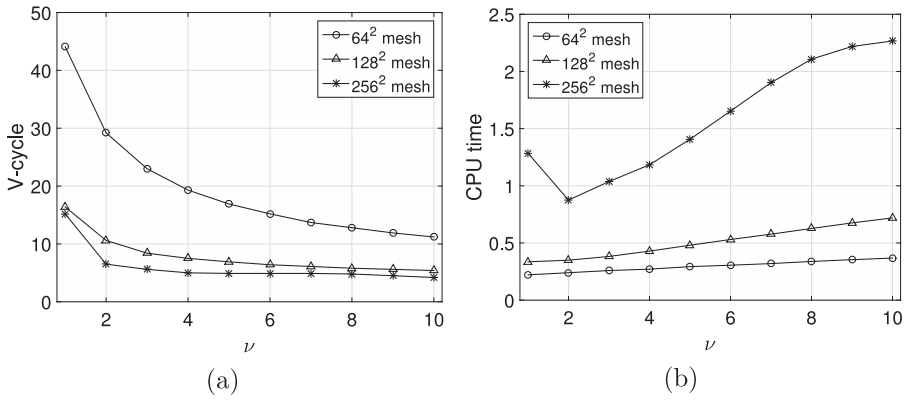

Fig. 12. (a) The number of V-cycles and (b) CPU time (in seconds) versus ν with the various mesh sizes.

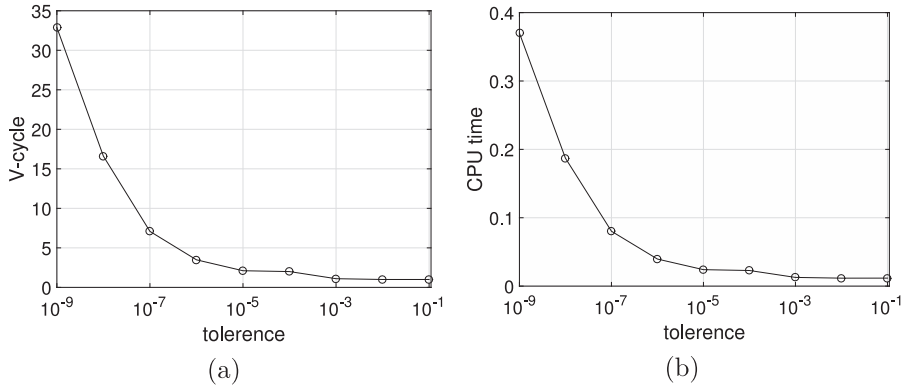

Fig. 13. (a) The number of V-cycles and (b) CPU time (in seconds) versus *tol*.

3.4. Effect of SMOOTH relaxation operator number ν

In this section, we show the relation between *SMOOTH* relaxation operator number ν and CPU time on the nonuniform grid in two-dimensional space. Also, we check average number of V-cycle for each value of ν. We run 10 iterations. In this simulation, we use the same initial condition and parameters in Fig. 11 except the value of ν. Fig. 12(a) shows that when the value of ν is increasing, the number of V-cycles is decreasing. However, as shown in Fig. 12(b), the CPU time is increasing. In a relatively find mesh, 256^2, the curve of the CPU time is not monotone. There is an optimal relaxation number, 2. Therefore, we use the *SMOOTH* relaxation operator number from $\nu = 3$ to $\nu = 5$ for the computational efficiency.

3.5. Effect of tolerance, tol

Next, we study the relation between tolerance (*tol*) and average number of V-cycles on the nonuniform grid in two-dimensional space. Also, we check the CPU time in seconds. We use various values of *tol* with the same initial condition and parameters as in Fig. 11. From Fig. 13, we can see that the number of V-cycles and the CPU times are inversely proportional to the value of *tol*.

3.6. Effect of time step Δt

We measure the iteration of V-cycle and CPU time for various Δt. Initial condition and other parameters are the same as in Fig. 11. When the time step size Δt is large, the number of V-cycle iterations and the CPU time in seconds increase as shown in Fig. 14.

3.7. Three-dimensional space

We discretize Eqs. (1) and (2) in time by a nonlinear splitting algorithm:

$$\frac{\phi_{ijk}^{n+1} - \phi_{ijk}^{n}}{\Delta t} = \Delta_d \mu_{ijk}^{n+1}, \ \ 1 \le i \le N_x, \ \ 1 \le j \le N_y, \ \ 1 \le k \le N_z, \ \ n \ge 0, \tag{22}$$

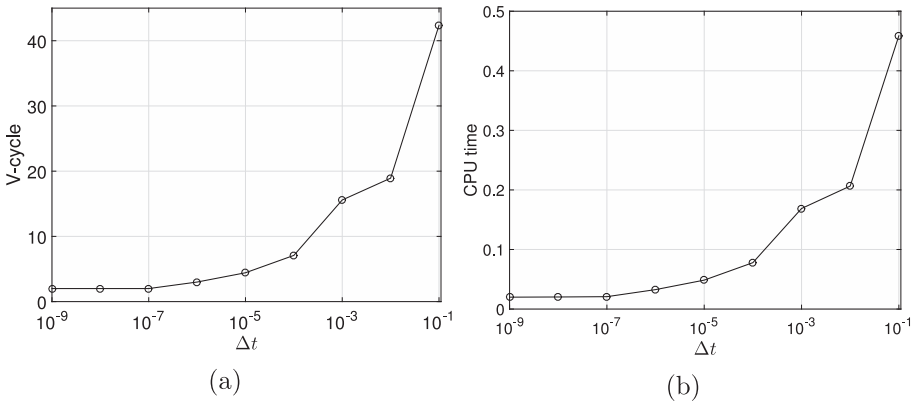

Fig. 14. (a) The number of V-cycles and (b) CPU time (in seconds) versus Δt.

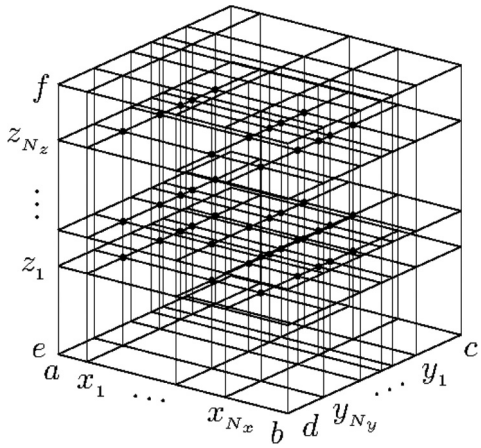

Fig. 15. Schematic illustration of a nonuniform grid on the three-dimensional space $\Omega = (a, b) \times (c, d) \times (e, f)$.

$$\mu_{ijk}^{n+1} = (\phi_{ijk}^{n+1})^3 - \phi_{ijk}^n - \epsilon^2 \Delta_d \phi_{ijk}^{n+1}, \tag{23}$$

where the discrete Laplacian is defined as

$$\begin{aligned}\Delta_d \phi_{ijk} = &\frac{2(\phi_{i+1,jk} - \phi_{ijk})}{h_i^x (h_i^x + h_{i-1}^x)} - \frac{2(\phi_{ijk} - \phi_{i-1,jk})}{h_{i-1}^x (h_i^x + h_{i-1}^x)} + \frac{2(\phi_{i,j+1,k} - \phi_{ijk})}{h_j^y (h_j^y + h_{j-1}^y)} \\ &- \frac{2(\phi_{ijk} - \phi_{i,j-1,k})}{h_{j-1}^y (h_j^y + h_{j-1}^y)} + \frac{2(\phi_{ij,k+1} - \phi_{ijk})}{h_k^z (h_k^z + h_{k-1}^z)} - \frac{2(\phi_{ijk} - \phi_{ij,k-1})}{h_{k-1}^z (h_k^z + h_{k-1}^z)}.\end{aligned} \tag{24}$$

Here, h_k^z is the nonuniform space step size in the z-direction. Fig. 15 shows a schematic illustration of a nonuniform grid in three-dimensional space.

We define the discrete energy functional as

$$\begin{aligned}\mathcal{E}_d(\boldsymbol{\phi}^n) = &\frac{1}{8} \sum_{i=1}^{N_x} \sum_{j=1}^{N_y} \sum_{k=1}^{N_z} F(\phi_{ijk}^n)(h_{i-1}^x + h_i^x)(h_{j-1}^y + h_j^y)(h_{k-1}^z + h_k^z) \\ &+ \frac{\epsilon^2}{2} \sum_{i=1}^{N_x - 1} \sum_{j=1}^{N_y - 1} \sum_{k=1}^{N_z - 1} \left[\frac{h_j^y h_k^z}{h_i^x} (\phi_{i+1,jk}^n - \phi_{ijk}^n)^2 + \frac{h_i^x h_k^z}{h_j^y} (\phi_{i,j+1,k}^n - \phi_{ijk}^n)^2 + \frac{h_i^x h_j^y}{h_k^z} (\phi_{ij,k+1}^n - \phi_{ijk}^n)^2 \right]\end{aligned} \tag{25}$$

and the total mass as

$$\mathcal{M}_d(\boldsymbol{\phi}^n) = \frac{1}{8} \sum_{i=1}^{N_x} \sum_{j=1}^{N_y} \sum_{k=1}^{N_z} \phi_{ijk}^n (h_{i-1}^x + h_i^x)(h_{j-1}^y + h_j^y)(h_{k-1}^z + h_k^z). \tag{26}$$

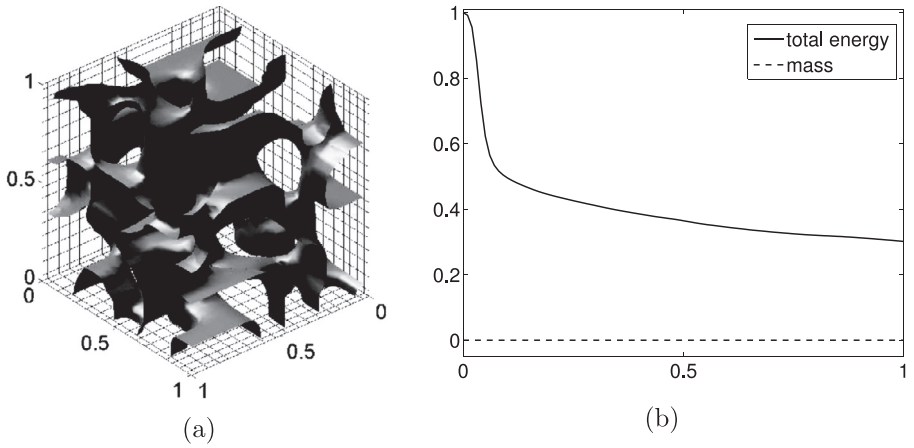

Fig. 16. (a) A snapshot of ϕ at $t = 80\Delta t$ with the initial condition $\phi(x, y, z, 0) = 0.1\text{rand}(\ )$. (b) Discrete total energy $\mathcal{E}_d(\boldsymbol{\phi}^n)/\mathcal{E}_d(\boldsymbol{\phi}^0)$ (solid line) and the total mass (dashed line) of the numerical solutions.

Table 3
List of parameters for numerical simulations.

Case	Initial condition	Domain	Δt	N_t	h_f	ϵ
1D	Fig. 5(c)	(0, 1)	0.01	1000	1/144	0.0075
2D	Fig. 11(a)	$(0, 1)^2$	0.0001	300	1/512	0.0019
3D	Fig. 17(a)	$(0, 1)^3$	0.01	1000	1/128	0.0075

Table 4
Average number of V-cycles and average CPU time per iteration.

	Aver. #V-cycle		Aver. CPU time			
Case	UMG	NMG	UGS	NGS	UMG	NMG
1D	1.3600	1.7167	6.7333e−4	1.0333e−4	5.2000e−4	1.0333e−4
2D	3.2967	6.0867	8.0598e−0	0.1046e−0	2.9576e−0	0.0765e−0
3D	3.1410	4.8370	384.9715e−0	46.2913e−0	28.6154e−0	5.6378e−0

3.7.1. Spinodal decomposition

We perform a spinodal decomposition simulation on a unit cube $\Omega = (0, 1) \times (0, 1) \times (0, 1)$ with a mesh of $32 \times 32 \times 32$ grid points, $\Delta t = 0.01$, $\epsilon = 0.0192$, and a randomly distributed nonuniform grid spacing. Fig. 16(a) shows a snapshot of ϕ at $t = 80\Delta t$ with the initial condition $\phi(x, y, z, 0) = 0.1\text{rand}(\ )$, where rand( ) is the random number between -1 and 1. Fig. 16(b) shows temporal evolutions of the normalized discrete total energy $\mathcal{E}_d(\boldsymbol{\phi}^n)/\mathcal{E}_d(\boldsymbol{\phi}^0)$ (solid line) and the total mass (dashed line) of the numerical solutions. The discrete energy is decreasing and the total mass is conserved.

3.7.2. Locally refined 3D grid

The first and the second rows in Fig. 17 represent the evolutions of a modified cube in three-dimensional space with uniform ($128 \times 128 \times 128$) and nonuniform ($64 \times 64 \times 64$) grids, respectively. Fig. 17(i) is the normalized discrete total energies and total masses with respect to time. In this simulation, the parameters are $\epsilon = 0.007493$ and $\Delta t = 0.01$ on a computational domain of $\Omega = (0, 1) \times (0, 1) \times (0, 1)$. The find grid size in the nonuniform mesh is same to the uniform mesh. We obtain the almost same results from both grid systems.

3.7.3. Efficiency test on the various dimensions

In this section, we evaluate the efficiency by comparing the averaged CPU time in seconds and the average number of multigrid cycles for the four cases, which are uniform Gauss–Seidel (UGS), nonuniform Gauss–Seidel (NGS), uniform multigrid (UMG), and nonuniform multigrid (NMG).

The initial conditions and parameters used to show the efficiency are listed in Table 3. Common parameters are *SMOOTH* relaxation operator step $\nu = 3$ and a given tolerance $tol = 1.0\text{e}{-7}$. Here, N_t is the number of the total iteration time steps.

In Table 4, the average number of V-cycles and the average CPU time, i.e.,

$$\text{Aver.\#V} - \text{cycle} = \frac{\text{Total \#V} - \text{cycle}}{N_t}, \qquad \text{Aver.CPUtime} = \frac{\text{Total CPU time}}{N_t}.$$

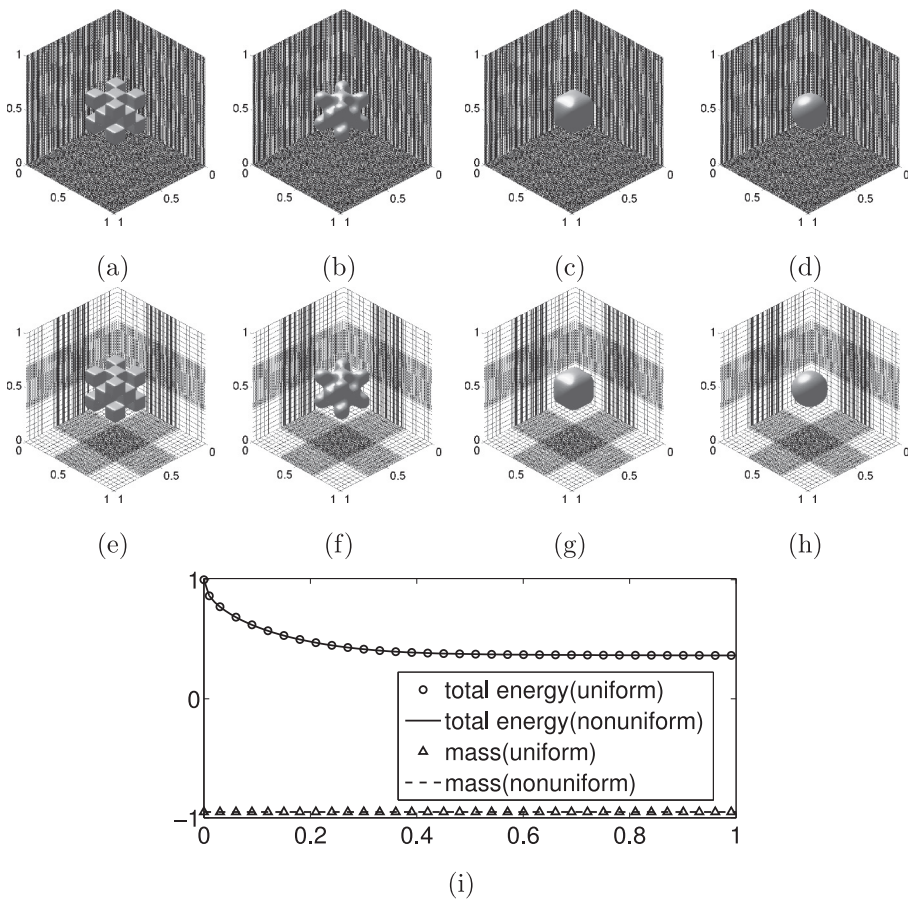

Fig. 17. (a) and (e) are the initial conditions on a uniform grid ($128 \times 128 \times 128$) and nonuniform grid ($64 \times 64 \times 64$), respectively. (b) and (f) are at $t = 10\Delta t$, (c) and (g) are at $t = 50\Delta t$, (d) and (h) are at $t = 1000\Delta t$. (i) is the normalized discrete total energies and total masses with respect to time.

are listed. We can confirm that NMG's CPU times are smaller than those from other three cases (UGS, NGS, UMG). Therefore, nonuniform multigrid method is efficient when compared with other techniques.

4. Conclusions

In this paper, we developed a nonlinear multigrid method for solving the CH equation on nonuniform grids. We applied an unconditionally gradient stable type scheme for the temporal discretization and a conservative finite difference scheme for the spatial discretization. Various numerical results in the one-, two-, and three-dimensional spaces were presented to demonstrate the accuracy and effectiveness of the nonuniform grids for the CH equation. The results showed that the proposed method is a promising approach for the numerical computations of the CH equation on non-square domains and adaptive grid systems. In future research, the methodology introduced in this paper will be applied to crystal growth and tumor growth simulations by incorporating morphology-dependent adaptive grid structures.

Acknowledgments

The corresponding author (J.S. Kim) was supported by the National Research Foundation of Korea (NRF) grant funded by the Korea government (MSIP) (NRF-2014R1A2A2A01003683). The authors greatly appreciate the reviewers for their constructive comments and suggestions, which have improved the quality of this paper.

References

[1] J.W. Cahn, J.E. Hilliard, Free energy of a non-uniform system. I. interfacial free energy, J. Chem. Phys. 28 (1958) 258–267.
[2] W. Chen, C. Wang, X. Wang, S.M. Wise, A linear iteration algorithm for a second-order energy stable scheme for a thin film model without slope selection, J. Sci. Comput. 59 (2014) 574–601.
[3] S.M. Choo, S.K. Chung, Conservative nonlinear difference scheme for the Cahn–Hilliard equation, Comput. Math. Appl. 36 (1998) 31–39.
[4] D. Furihata, A stable and conservative finite difference scheme for the Cahn–Hilliard equation, Numer. Math. 87 (2001) 675–699.

[5] R. Guo, Y. Xu, Efficient solvers of discontinuous Galerkin discretization for the Cahn–Hilliard equations, J. Sci. Comput. 58 (2014) 380–408.
[6] E.V.L. Mello, O.T.d. S. Filho, Numerical study of the Cahn–Hilliard equation in one, two and three dimensions, Physica A 347 (2005) 429–443.
[7] T.M. Rogers, R.C. Desai, Numerical study of late-stage coarsening for off-critical quenches in the Cahn–Hilliard equation of phase separation, Phys. Rev. B 39 (1989) 956–964.
[8] Z.Z. Sun, A second-order accurate linearized difference scheme for the two-dimensional Cahn–Hilliard equation, Math. Comput. 64 (1995) 1463–1471.
[9] H.D. Ceniceros, A.M. Roma, A nonstiff, adaptive mesh refinement-based method for the Cahn–Hilliard equation, J. Comput. Phys. 225 (2007) 1849–1862.
[10] J. Kim, H.O. Bae, An unconditionally gradient stable adaptive mesh refinement for Cahn–Hilliard equation, J. Korean Phys. Soc. 53 (2008) 672–679.
[11] S. Wise, J. Kim, J. Lowengrub, Solving the regularized, strongly anisotropic Cahn–Hilliard equation by an adaptive nonlinear multigrid method, J. Comput. Phys. 226 (2007) 414–446.
[12] Y. Ge, F. Cao, J. Zhang, A transformation-free HOC scheme and multigrid method for solving the 3D Poisson equation on nonuniform grids, J. Comput. Phys. 234 (2013) 199–216.
[13] M. Saraniti, A. Rein, G. Zandler, P. Vogl, P. Lugli, An efficient multigrid Poisson solver for device simulations, IEEE Trans. Comput. Aided Des. Int. Circuits Syst. 15 (1996) 141–150.
[14] F. Liu, A. Jameson, Cascade flow calculations by a multigrid Euler method, J. Propuls. Power 9 (1993) 90–97.
[15] J.C. Mandal, H.S. Rajput, An improved multigrid method for Euler equations, Comput. Mech. 23 (1999) 397–403.
[16] R.K. Shukla, M. Tatineni, X. Zhong, Very high-order compact finite difference schemes on non-uniform grids for incompressible Navier–Stokes equations, J. Comput. Phys. 224 (2007) 1064–1094.
[17] P.X. Yu, Z.F. Tian, A compact stream function-velocity scheme on nonuniform grids for the 2D steady incompressible Navier–Stokes equations, Comput. Math. Appl. 66 (2013) 1192–1212.
[18] D.J. Eyre, Computational and Mathematical Models of Microstructural Evolution, The Material Research Society, Warrendale, PA, 1998.
[19] W.L. Briggs, V.E. Henson, S.F. McCormick, A Multigrid Tutorial, Society for Industrial and Applied Mathematics, Philadelphia, PA, 2000.
[20] U. Trottenberg, C. Oosterlee, A. Schüller, Multigrid, Academic Press, 2001.
[21] J.W. Choi, H.G. Lee, D. Jeong, J. Kim, An unconditionally gradient stable numerical method for solving the Allen–Cahn equation, Physica A 388 (2009) 1791–1803.